Applied Thermal Engineering 258 (2025) 124622

Contents lists available at ScienceDirect

Applied Thermal Engineering

journal homepage: www.elsevier.com/locate/apthermeng

Research Paper

Energy conversion performance in looped and stirling traveling-wave and standing-wave thermoacoustic engines

Lixian Guo [a], Dan Zhao [a,*], Guoyao Yu [b], Jingyuan Xu [c], Yunpeng Su [a], Dakun Sun [d], Yue Zhang [e]

[a] Department of Mechanical Engineering, Faculty of Engineering, University of Canterbury, Private Bag 4800, Christchurch 8041, New Zealand
[b] Technical Institute of Physics and Chemistry, Chinese Academy of Sciences, Beijing 100190, China
[c] Institute of Microstructure Technology, Karlsruhe Institute of Technology, Karlsruhe 76344, Germany
[d] Fluid and Acoustics Engineering Laboratory, School of Energy and Power Engineering, Beihang University, Beijing, 100191, China
[e] College of Energy and Power Engineering, Nanjing University of Aeronautics and Astronautics, Nanjing 210016, China

ARTICLE INFO

Keywords:
Thermoacoustics
Thermoacoustic engine
Traveling-wave
Thermodynamics
Heat transfer
Nonlinear dynamics

ABSTRACT

This present study conducts a comprehensive comparison of looped traveling-wave thermoacoustic engines (TWTAEs) and Stirling TWTAEs using two- and three-dimensional (2D and 3D) time-domain models. These models, validated through comparisons with existing experimental results, confirm the accuracy of our developed full-scale numerical TWTAE models. By evaluating the acoustic characteristics and comparing them with conventional standing-wave thermoacoustic engines, this work highlights the superior performance of the Stirling TWTAE. It achieves the highest heat-driven acoustic power and thermoacoustic energy conversion efficiency. This superior performance is attributed to its operation at a lower oscillation frequency (115 Hz) and an optimized phase between acoustic velocity and pressure oscillations (40 degrees). Additionally, our study explores rich nonlinear phenomena within the flow fields of the Stirling TWTAE. Notably, varying the temperature gradients between 410 K and 485 K introduces a bistable zone with distinct pressure amplitudes. Moreover, mass streaming under varying temperature gradients, and mode transitions due to external flow perturbations are observed inside the engine. These findings not only quantitatively confirm the high efficiency potential of the Stirling TWTAE but also demonstrate the effectiveness of CFD in the development of full-scale numerical models for predicting and optimizing the heat-driven acoustic characteristics and nonlinear phenomena of traveling-wave thermoacoustic systems.

1. Introduction

With the rise in global temperatures and ongoing climate change, there is an increasing focus on sustainable development and environmental protection [1]. This has driven research into renewable energy sources and improved energy efficiency to reduce reliance on fossil fuels and curb greenhouse gas emissions [2,3]. Among the alternative solutions, the thermoacoustic engine (TAE) has gained considerable attention due to its potential to address the challenges posed by traditional energy sources through efficient energy conversion [4,5]. TAEs convert heat energy into acoustic energy, utilizing low-grade thermal energy sources such as industrial waste heat or renewable energy like solar power [6–8]. TAEs are broadly categorized into standing-wave TAEs (SWTAEs) and traveling-wave TAEs (TWTAEs), distinguished by the phase difference between pressure and velocity oscillations [9,10]. Notably, TWTAEs offer higher theoretical energy conversion efficiency due to their reversible heat conduction properties [11–13].

Ceperley [14,15] proposed the concept of the looped-tube-type TWTAE (looped TWTAE) in 1979, providing valuable insights into enhancing the efficiency of TAEs. In 1997, Yazaki et al. [3] constructed a looped TWTAE and successfully observed the acoustic oscillations. In 1999, Backhaus and Swift [16,17] developed the Stirling-type TWTAE (Stirling TWTAE), achieving a sound power of 710 W and thermal efficiency of about 30 %, comparable to traditional internal combustion engines. Luo et al. [18,19] extended these studies by investigating the influence of geometric dimensions and operational parameters on Stirling TWTAE performance, achieving a pressure ratio of 1.40 using nitrogen at 1.5 MPa. Furthermore, Xiao et al. [20,21] conducted extensive research on thermoacoustic refrigeration powered by TWTAEs, achieving refrigeration power in the kilowatt range. Hsu et al. [22–24] explored the effects of liquid columns, diaphragms, and condensation

* Corresponding author.
E-mail address: dan.zhao@canterbury.ac.nz (D. Zhao).

https://doi.org/10.1016/j.applthermaleng.2024.124622
Received 24 June 2024; Received in revised form 8 September 2024; Accepted 10 October 2024
Available online 12 October 2024

Nomenclature

A	Cross-sectional area [m^2]
C_p	Isobaric specific heat [J/kg·K]
D	Engine diameter [mm]
E	Total energy [J]
$\dot{E}_f$	Forcing power of the external perturbations [W]
e	Internal energy [J]
F(t)	Oscillation growth rate function
f_{Rn}	n^{th}-order acoustic oscillation frequency [Hz]
f_{Rd}	Dominant oscillation frequency [Hz]
f_s	Self-excited frequency of the TAE [Hz]
f_f	Forced frequency [Hz]
h	The surface heat transfer coefficient [W/m^2·K]
$I(\omega)$	Acoustic power [W]
$\widehat{I}_{1A}(\omega)$	Fundamental-mode acoustic power amplitude [W]
k	Turbulence kinetic energy
L	Length of the engine [m]
L_L	Looped tube length [m]
L_R	Resonator length [m]
p	Pressure [Pa]
p_f	Forced periodic pressure
p'	Acoustic oscillation pressure [Pa]
$p_{A'}$	The limit cycle oscillations' velocity amplitude [Pa]
p_a	Initial pressure [Pa]
$\widehat{p}_{LFM}$	The pressure amplitude at low frequency-mode [Pa]
$\widehat{p}_{HFM}$	The pressure amplitude at high-frequency mode [Pa]
$\widehat{p}_{nA}$	n^{th}-order pressure amplitudes of the decomposed oscillation pressure [Pa]
$\dot{q}_t$	Transversal heat flux [W/m^2]
$\dot{Q}_{in}$	Input heat power [W]
$\dot{Q}_{out}$	Output heat power [W]
R	Gas constant [J/K • kg]
T	Gas temperature [K]
T_h	Hot end temperature of the regenerator [K]
T_c	Cold end temperature of the regenerator [K]
T_w	Wall temperature of the regenerator [K]
t	Time [s]
t_0	Time step [s]
t_{ls}	Regenerator thickness of the looped thermoacoustic engine [mm]
t_{lp}	Plate spacing of the looped thermoacoustic engine [mm]
t_{ss}	Regenerator thickness of the Stirling thermoacoustic engine [mm]
t_{sp}	Plate spacing of the Stirling thermoacoustic engine [mm]
v	Velocity [m/s]
v_f	Forced periodic velocity
v'_A	The limit cycle oscillations' velocity amplitude [m/s]
Δwz	Cell volume
$\overline{\rho v}$	Time-averaged air mass flow rate [kg/m^2 • s]

Greek symbols

α	Any instantaneous thermodynamic variable
$\overline{\alpha}$	Time-averaged component of any instantaneous thermodynamic variable
α'	Fluctuating component of any instantaneous thermodynamic variable
$\widehat{\alpha}_n$	n^{th}-order components of any instantaneous thermodynamic variable after Fast Fourier Transform algorithm analysis
ε	Turbulent dissipation
τ	Time required for thermal equilibrium [s]
ΔT_{cri}	Onset temperature gradient [K]
ω	Angular frequency [rad/s]
δ_g	Oscillation growth rate
τ_{ij}	Viscous stress tensor [Pa]
μ	Dynamic viscosity [m^2/s]
μ_t	Turbulence viscosity [m^2/s]
σ_T	Turbulence Prandtl number
ϑ	Thermal diffusivity
θ	Phase lead of the limit cycle oscillation's velocity to pressure
η	Thermal efficiency
κ	Thermal conductivity [W/m·K]
ρ	Density of fluid [kg/m^3]
φ	Phase over a complete acoustic period/cycle

Abbreviation

CFD	Computational Fluid Dynamics
CFL	Courant-Friedrichs-Lewy Number
FFT	Fast Fourier Transform
LES	Large Eddy Simulation
TAE	Thermoacoustic Engine
SWTAE	Standing-wave Thermoacoustic Engine
TWTAE	Traveling-wave Thermoacoustic Engine
UDF	User Defined Function
URANS	Unsteady Reynolds Averaged Navier Stokes

shocks on Stirling TAEs, focusing on enhancing system performance through impedance matching and refining modeling techniques for operational conditions. Recently, Zera et al. [25–27] conducted extensive studies on the coupling effects of the Stirling TWTAE, focusing on the modeling, construction, and optimization of its acoustic characteristics by investigating the startup (onset point) and stable limit cycle (steady-state) conditions.

While experimental research has provided a foundation for understanding TAEs, Computational Fluid Dynamics (CFD) has emerged as a powerful tool for investigating complex behaviors that are difficult to observe experimentally [28,29]. CFD has been validated as an effective tool for investigating the inside flow fields of thermoacoustic systems [30,31]. The first CFD simulation of a TWTAE was performed by Lycklama et al. [32,33], who identified streaming effects caused by oscillating flow in the T-junction of a torus-shaped engine, suggesting streamlined designs to mitigate these effects. Yang et al. [34] introduced a time-domain Stirling TWTAE model with a short tube, concluding that increasing the diameter can reduce power dissipation and improve energy conversion efficiency.

However, to the authors' best knowledge, CFD applications in the study of TWTAEs still need improvement [35]. Firstly, most existing CFD studies on TWTAEs involve truncated computational domains and simplified boundary conditions [36]. This is due to the TWTAE's inherently complex geometric structure and larger model dimensions, which require high grid resolution and extended simulation times. These simplified models deviate from reality, limiting their practical application. To address these gaps, this study first develops full-scale two- and three-dimensional (2D and 3D) time-domain models for both looped and Stirling TWTAEs and validates them against existing experimental data. Secondly, while TWTAEs are theoretically more efficient than SWTAEs, practical and comparative performance data are lacking. This study conducts a detailed comparative analysis of looped TWTAE, Stirling TWTAE, and SWTAE performances under identical operating conditions. By comparing their acoustic characteristics, thermoacoustic conversion efficiencies, and internal flow dynamics, this approach provides a quantitative evaluation of each engine's performance. Thirdly, due to

the lack of appropriate numerical models, research on the nonlinear effects within the internal flow fields of Stirling TWTAEs and their impact on acoustic performance is limited. Therefore, this study aims to analyze the internal flow fields of Stirling TWTAEs to understand how various operational conditions influence the nonlinear effects within these fields. This study uniquely contributes to the field by providing full-scale, validated CFD models for TWTAEs, conducting quantitative performance comparisons across TAE types, and exploring the nonlinear

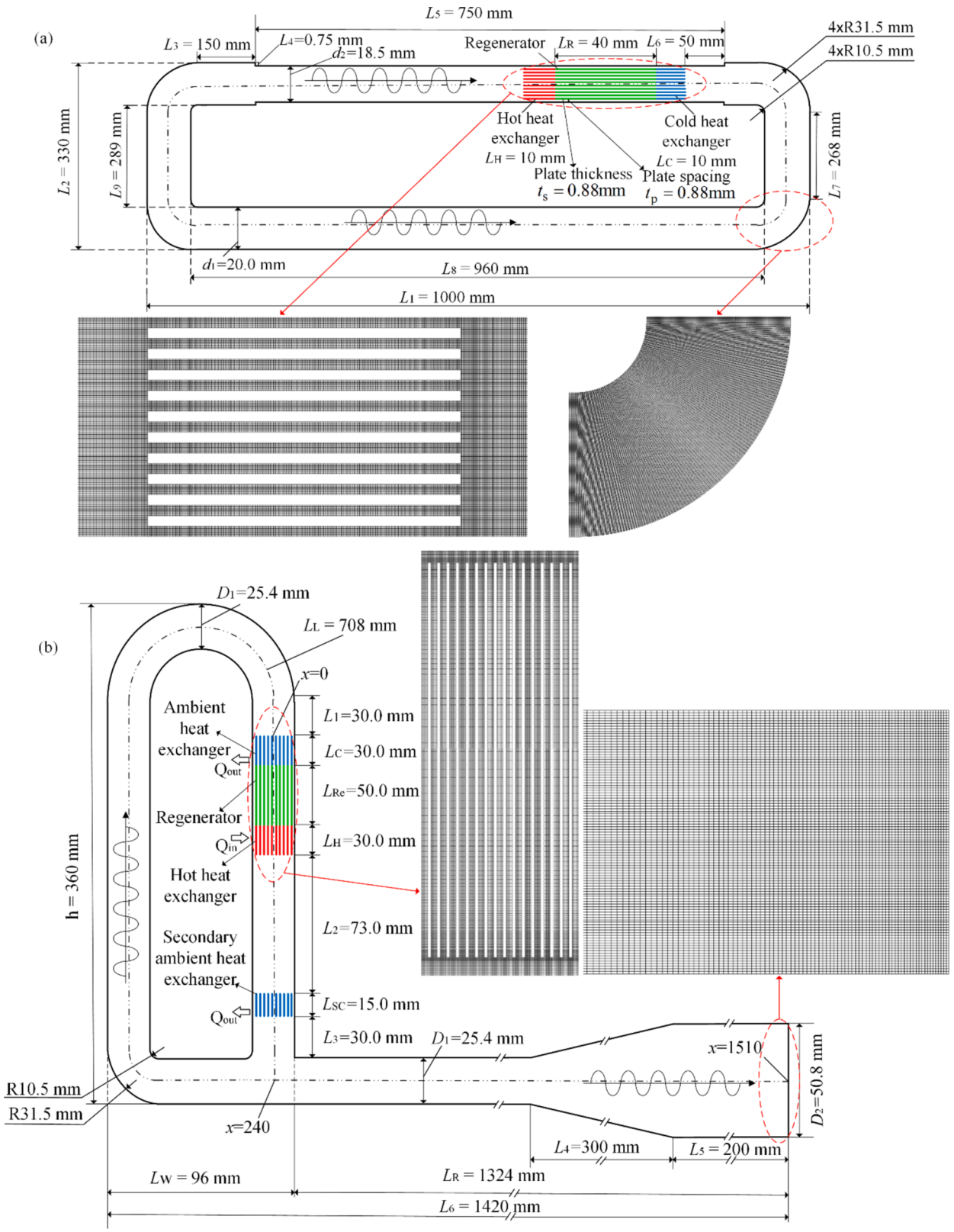

Fig. 1. The 2D computational domain of the full scale (a) looped TWTAE based on the experimental study [3], with the mesh configurations in the regenerator and bend regions, and (b) Stirling TWTAE based on the experimental study [10], with the mesh configurations in the regenerator and resonator regions.

dynamics within the flow fields of Stirling TWTAEs.

The rest of this paper is structured as follows: Section 2 presents the development of numerical looped and Stirling TWTAE models, including model validations and a comparative analysis with experimental results from the literature. Section 3 compares the acoustic output characteristics and inside flow fields of different TAE types with consistent dimensional parameters. The nonlinear effects exhibited by the TAE under different operational conditions are investigated in Section 4. Concluding remarks are provided in Section 5.

2. Numerical Methodology

2.1. Description of the looped and Stirling TWTAE numerical models

The 2D full-scale numerical looped TWTAE model is established based on the experiments of Yazaki et al. [3]. The computational domain and geometric dimensions of the looped TWTAE model are shown in Fig. 1(a). High-quality structured meshes are generated for the computational domain in ICEM, with particular emphasis on critical regions such as the regenerator and tube bends, as depicted in Fig. 1(a). To adequately capture the dynamic effects associated with wall boundary flows, the maximum dimension in the normal direction is set at 0.1 mm. According to the looped TWTAE model from the previous experiment in Ref. [3], the mean length of the looped tube is approximately 2600 mm, with an inner radius of 20.0 mm, reduced to 18.5 mm in certain parts. The TAE model consists of a looped tube in which the regenerator is placed between the two heat exchangers. The temperatures of the hot and cold exchangers are maintained at T_h and T_c, with T_h and T_c set to 640 K, and 300 K, respectively. The regenerator is 40 mm long, consisting of ten parallel plates in the axial direction with a regenerator thickness t_s and plate spacing t_p equal to 0.88 mm. The working medium/gas is air with a temperature of 300 K and an average atmospheric pressure of 101,325 Pa.

Moreover, the 2D full-scale numerical Stirling TWAE model is established based on the experiments by Wu et al. [10]. The computational domain and geometric dimensions of the Stirling TWTAE model are shown in Fig. 1(b). The Stirling TWTAE is consisted of a looped tube with a center axis of length $L_L = 708$ mm and an acoustic resonator of $L_R = 1324$ mm. The regenerator, composed of wire screens in the experiment, is modeled using parallel plates in the simulation. This approach is adopted due to the near-zero average velocity in the internal flow field of the TWTAE, resulting in an extremely low Mach number. Consequently, suboptimal simulation outcomes occur when using the porous media module in ANSYS Fluent, as it struggles to accurately simulate such low Mach number conditions [37]. Referring to the aluminum steel wire mesh heat exchanger with a porosity of 60 %-80 % [38], the designed regenerator consists of 16 parallel plates, each with a thickness of 0.53 mm, achieving an approximate porosity of 70 % [39]. The inlet diameter and length of the regenerator are 25.4 mm and 32 mm, respectively. The working gas is nitrogen at an operating pressure of 0.8 MPa, with an input heat power of 270 W in the experiment.

2.2. Governing equations and boundary conditions of the TWTAE models

In previous studies, Yu et al. [35] and Yang et al. [34] successfully employed the standard k-ε model to simulate the viscous and turbulent effects of the TWTAE. This research continues to use the standard k-ε model of URANS (Unsteady Reynolds Averaged Navier-Stokes). In Reynolds averaging, the thermodynamic variables (α) are decomposed into the time-averaged and fluctuating components, expressed as $\alpha = \overline{\alpha} + \alpha'$, where $\overline{\alpha}$ and α' are the mean and fluctuating components, respectively. For compressible flows, a density-weighted time-average decomposition is applied. The variables can then be expressed as $\widetilde{\alpha} = \overline{\rho\alpha}/\overline{\rho}$ and $\alpha = \widetilde{\alpha} + \alpha''$, where $\widetilde{\alpha}$ and α'' are the mean and fluctuating parts. The governing equations are formulated as follows:

$$\frac{\partial \overline{\rho}}{\partial t} + \frac{\partial\left(\overline{\rho}\widetilde{v}_i\right)}{\partial x_i} = 0 \tag{1a}$$

$$\frac{\partial\left(\overline{\rho}\widetilde{v}_i\right)}{\partial t} + \frac{\partial\left(\overline{\rho}\widetilde{v}_i\widetilde{v}_j\right)}{\partial x_j} = -\frac{\partial \overline{p}}{\partial x_i} + \frac{\partial}{\partial x_j}\left(\widetilde{\tau}_{ij} - \overline{\rho}\overline{v_i'' v_j''}\right) \tag{1b}$$

$$\frac{\partial}{\partial t}\left(\overline{\rho}\widetilde{E}\right) + \frac{\partial}{\partial x_i}\left(\overline{\rho}\widetilde{v}_i\widetilde{h}_t\right) = \frac{\partial}{\partial x_i}\left(\kappa\frac{\partial \widetilde{T}}{\partial x_i} - \overline{\rho}\overline{v_i'' T''} + 2\tau_{ij}''\widetilde{v}_j - \overline{\rho}\overline{v_i'' v_j''}\widetilde{v}_j\right) \tag{1c}$$

where ρ, t, p, v, κ and x stand for density, time, pressure, velocity, thermal conductivity and spatial dimension, respectively. The indices i and j represent the Cartesian coordinate directions. E and τ_{ij} are total energy and viscous stress tensor, respectively, expressed as:

$$E = e + \frac{1}{2}v_j v_j \tag{2a}$$

$$\tau_{ij} = \mu\left(\frac{\partial v_i}{\partial x_j} + \frac{\partial v_j}{\partial x_i}\right) - \frac{2}{3}\mu\frac{\partial v_k}{\partial x_k} \tag{2b}$$

where μ, e and δ_{ij} are the dynamic viscosity, specific internal energy and Kronecker delta function, respectively. The system remains unclosed due to the unknown Reynolds stress tensor ($\overline{v_i'' v_j''}$) and the turbulent heat vector ($\overline{v_i'' T''}$). To model the effect of turbulence on the flow, the Boussinesq hypothesis is applied [30]:

$$\overline{v_i'' v_j''} = -\frac{\mu_t}{\mu}\widetilde{\tau}_{ij} + \frac{2}{3}k\delta_{ij} \tag{3a}$$

$$\overline{v_i'' T''} = -\frac{\mu_t}{\sigma_T}\frac{\partial \overline{T}}{\partial x_i} \tag{3b}$$

where k, μ_t, and σ_T are the turbulence kinetic energy, turbulence viscosity, and turbulence Prandtl number, respectively.

In the standard k-ε model, μ_t is computed from turbulence kinetic energy (k) and turbulent dissipation (ε) [30]. The k-ε model is resolved in the CFD solver ANSYS Fluent 2022 R2. The working gas is treated as an ideal gas, and gravity effects are neglected, expressed as $p = \rho RT$, where R is the gas constant ($287 J/K \bullet kg$). Numerical solutions are obtained using the Pressure-Velocity Coupling algorithm, chosen for its low computational cost in highly thermo-viscous coupling systems. To ensure simulation accuracy, the Second Order Upwind Scheme is applied to all flow variables. The PISO algorithm, Least Squares Cell-Based gradient evaluation, and PRESTO! scheme are employed for pressure calculations. To ensure convergence, the relaxation factors for pressure, density, body forces, momentum, turbulence kinetic energy, turbulence dissipation rate, turbulent viscosity, and energy are set to 0.3, 1, 1, 0.7, 0.8, 0.8, 1, and 1, respectively.

2.3. Mesh- and time-independence studies

The CFD simulation results for the TWTAEs must remain consistent, unaffected by variations in the number of meshes and time steps. Zarch et al. [40] conducted an analysis of the heat transfer characteristics and nonlinear phenomena in thermoacoustic devices, emphasizing that heat convergence is a critical convergence criterion. Although ideal heat exchange in traveling-wave systems is isothermal, there is still a temperature difference between the wall temperature of the regenerator (T_w) and the average temperature of the working gas ($\overline{T}$) in practical traveling wave thermoacoustic engines. In the regenerator area, heat fluxes in the transverse direction at the solid surfaces due to heat diffusion. The time-averaged transversal heat flux ($\dot{q}_t$) can be calculated as

$$\dot{q}_t = -\kappa \frac{\partial \overline{T}}{\partial n}\bigg|_{surface} = h(T_w - T_m) \quad (4)$$

where n is the direction perpendicular to the wall, and h is the surface heat transfer coefficient derived from CFD. $\dot{q}_t$ at the hot end of the regenerator is used as the key metric for assessing mesh and time-independence, as shown in Fig. 2. Fig. 2(a) illustrates the $\dot{q}_t$ of the looped TWTAE is initially increased and tended to 'saturate' from the 6×10^5 group. Therefore, the 6×10^5 group is selected for the looped TWTAE. Meanwhile, the $\dot{q}_t$ of the Stirling TWTAE is stabilized from the 5×10^5 group, making 5×10^5 the optimal number of nodes for the Stirling TWTAE. Moreover, simulations are implemented on the TWTAE models with six different time steps, i.e., 0.25×10^{-5} s, 0.5×10^{-5} s, 1.0×10^{-5} s, 1.5×10^{-5} s, 2.0×10^{-5} s, and 5.0×10^{-5} s, respectively. Fig. 2(b) shows that $\dot{q}_t$ is stabilized in the first three groups and then decreased after 1.0×10^{-5} s in both looped and Stirling TWTAEs. The Courant-Friedrichs-Lewy (CFL) number, defined as $CFL = v' t_0 / \sqrt[3]{\Delta wz}$, where v', t_0 and Δwz are the acoustic oscillations' velocity, time step and cell volume, respectively, must be less than 1 to ensure reliable simulation results. Under this time step, the maximum CFL numbers of 0.75 and 0.8 are achieved for the looped and Stirling TWTAEs, respectively, ensuring the stability of the simulation results. Therefore, 1.0×10^{-5} s is selected as the optimal time step value for both looped and Stirling TWTAEs.

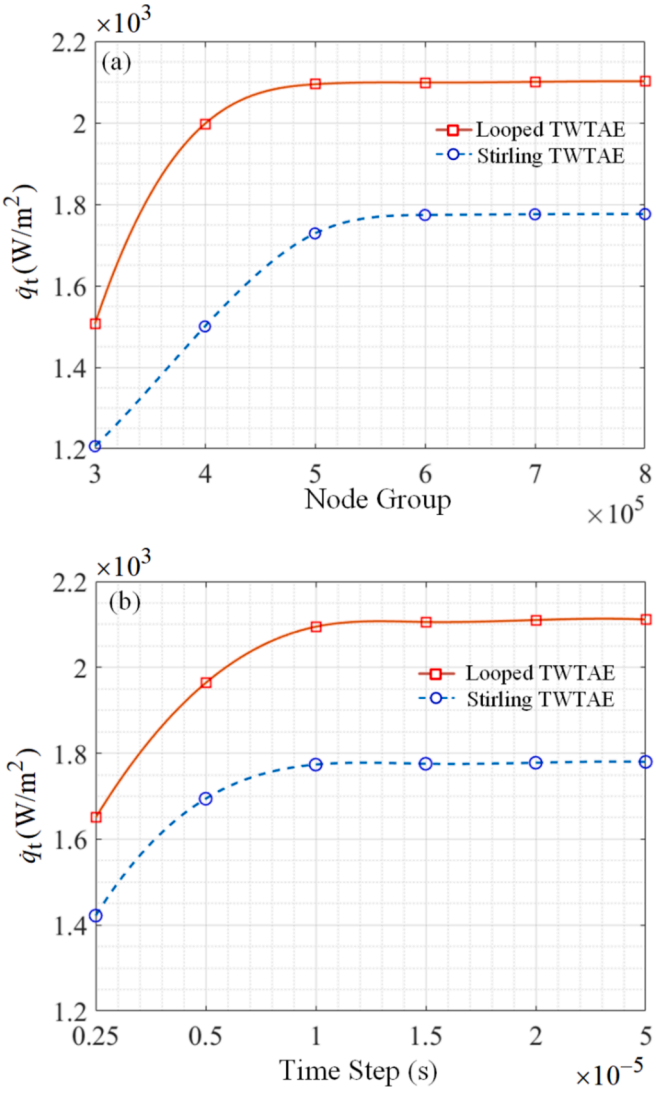

Fig. 2. Comparison results of the (a) mesh- and (b) time-independence of the looped and Stirling traveling-wave thermoacoustic engines.

2.4. Model validation of the TWTAEs predicted by different turbulence models

Full-scale 3D looped and Stirling TWTAE models with identical geometric dimensions are established to assess the impact of simplifying the 3D TWTAE system into a 2D system. The 3D simulations are conducted under the same settings and operational conditions with 2D simulations. All solid walls of the engine are set as adiabatic, and no-slip conditions are applied to rigid walls. Due to the complex structure of the 3D traveling-wave system, unstructured meshes are generated using the Fluent meshing tool. The finest mesh group of the 3D model is established, which requires 8.6×10^6 cells. The 3D TWTAE model is simulated using both LES and k-ε models, while the laminar model is also employed for the 2D TWTAE simulation.

The influence of different turbulence models on the simulation results of the TWTAE systems is evaluated in terms of acoustic characteristics and heat fluxes, as shown in Table 1. For the looped TWTAE, the acoustic power density generated by the regenerator ($\Delta I(\omega)/A$) from Fig. 3(b) of the corresponding study [3] is extracted. Since the regenerator is the primary site for thermoacoustic effects in these devices, the acoustic power generated by the regenerator $\Delta I(\omega)$ is obtained by calculating the difference in acoustic power between the hot and cold ends of the regenerator [41]. The acoustic power ($I(\omega)$) represents the capacity of energy conversion from heat energy to acoustic energy of the TAE. Given that higher-order acoustic power is negligible, the fundamental-mode acoustic power ($\widehat{I}_{1A}(\omega)$) is typically used to represent the heat-driven acoustic energy output of thermoacoustic devices. $\widehat{I}_{1A}(\omega)$ can be calculated as

$$\widehat{I}_{1A}(\omega) = \frac{1}{2}|\widehat{p}_{1A'}||\widehat{v}_{1A'}| A cos\theta_n \quad (5)$$

where θ_n and A is the phase lead of the limit cycle oscillation's velocity to pressure and cross-sectional area of the tube, respectively. The fluctuating pressure of the limit cycle oscillations (p'), obtained in the time domain, is subjected to Fast Fourier Transform (FFT) algorithm analysis to decompose it into the fundamental mode ($\widehat{p}_1$) and nth-order harmonic components ($\widehat{p}_n$) in the frequency domain. $|\widehat{p}_{1A'}|$and$|\widehat{v}_{1A'}|$ represent the maximum values of pressure and velocity, respectively, corresponding to the fundamental mode. For the Stirling TWTAE, we obtained the low frequency corresponding to the pressure values ($\widehat{p}_{LFM}$) at $x = 0$ from Fig. 8 in the corresponding study [10].

As shown in Table 1, a comparison with the experimental data indicates that $\Delta I(\omega)/A$ from the LES, 2D k-ε and 3D k-ε results are 11.5 %, 19.0 % and 16.0 % higher than the experimental value for the looped TWTAE, respectively. The 2D laminar model also shows proximity, with values approximately 5.5 % lower than the experimental data. Considering potential experimental losses, such as leakage, it is reasonable for the simulation data to be slightly higher than the experimental values. The trends in the predicted $\widehat{p}_{LFM}$ of the Stirling TWTAE across various turbulence models are consistent with those observed in the looped model. $\widehat{p}_{LFM}$ predicted by the 3D LES model remains the closest to the experimental value (24,820 Pa vs. 22,780 Pa), while the 2D laminar model predicts the lowest value (17,860 Pa). Therefore, LES is considered the most accurate turbulence model for this TWTAE model and is used as the reference value. Furthermore, when the instantaneous temperature oscillations reach the steady state, $\dot{q}_t$ predicted by different models is also obtained, as shown in Table 1. It can be observed that, in the looped and Stirling TAE models, the differences between the results predicted by the 2D k-ε model and those predicted by the LES model are within 9.5 %. This indicates that the k-ε model can effectively estimate the heat transfer characteristics of a typical thermoacoustic engine. This finding aligns with our previous conclusions regarding the systematic impact of turbulence models [42,43]. Therefore, the differences in

Table 1
Model validation through comparison of 2D and 3D looped and Stirling TWTAEs, evaluating the corresponding acoustic characteristics and heat fluxes simulated by using different turbulence models.

		2D laminar	2D k-ε	3D k-ε	3D LES	Experiment
Looped TWTAE	$\Delta I(\omega)/A$(W/m^2)	189	238	232	223	200
	$\dot{q}_t$(W/m^2)	1,480	1,774	1,726	1,656	–
Stirling TWTAE	$\hat{p}_{\mathrm{LFM}}$(Pa)	17,860	26,420	25,890	24,820	22,780
	$\dot{q}_t$(W/m^2)	1,686	2,095	1,749	1,897	–

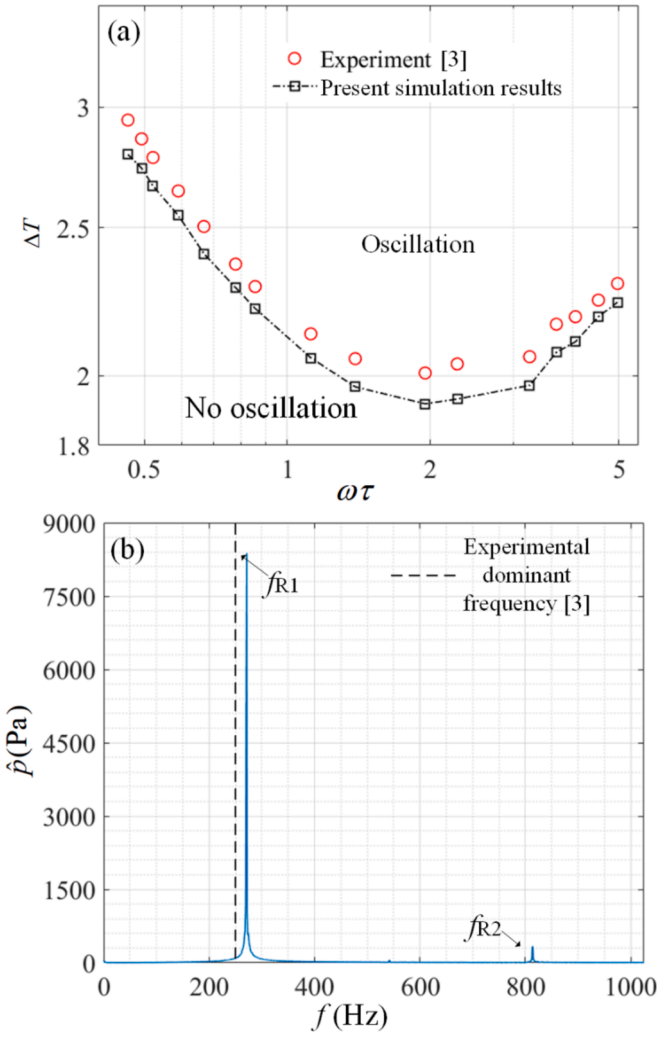

Fig. 3. Comparison of numerical and experimental results for the (a) onset temperature ratio between temperature gradient and $\omega\tau$ of the looped TWTAE, and (b) frequency spectrum of the acoustic pressure fluctuations and the corresponding experimental frequency of the looped TWTAE.

acoustic characteristics and heat fluxes between the 3D LES simulations and the 2D k-ε model are within an acceptable range. This result demonstrates that it is reasonable to approximate 3D oscillation characteristics using 2D reduced-order waves in looped and Stirling TWTAEs.

Note that the number of cells in the 3D looped TWTAE model is approximately 8.6×10^6, resulting in a 2186 % increase in the simulation time for the 3D k-ε model compared to the 2D k-ε model when simulating the looped TWTAE system for 10 s. Moreover, the 3D LES model leads to a 223 % increase in simulation time compared to the 3D k-ε model. Therefore, transitioning from 2D to 3D simulations for the looped TWTAE requires a significant investment of time in both modeling and computation. This finding also applies to Stirling TWTAE simulations. Considering both simulation costs and the comparison results, the 2D k-ε model is selected as the standard approach for predicting the acoustic oscillation characteristics of the TWTAE models in this study.

2.5. Comparison between the simulation and experimental results of the looped and Stirling TWTAEs

According to Yazaki et al. [3], the parameter $\omega\tau$ is a crucial controlled parameter in thermoacoustic energy conversion within the looped TWTAE [3]. Here, ω represents the angular frequency, while τ denotes the time required for thermal equilibrium in the TWTAE, signifying the time required for the system to reach a 'saturation' state. The time constant τ is obtained by the formula $\tau = r^2/2\vartheta$, where r is the characteristic transverse length of the channel (0.44 mm in this model). The thermal diffusivity $\vartheta = \kappa/C_p\overline{\rho}$ is the thermal diffusivity of gas; C_p denotes isobaric heat. The onset temperature gradient (ΔT_{cri}) is the critical temperature gradient at which self-sustained oscillations begin in the thermoacoustic system [22]. The onset temperature gradient (ΔT) is defined as the ratio of the hot-end temperature (T_h) to the cold-end (T_c) temperature of the regenerator. In the simulation, it is implemented by gradually increasing the hot-end temperature until the point of self-excited oscillation is reached. Ref. [3] provides a detailed discussion on the relationship between energy conversion and control parameters in the thermoacoustic system, particularly focusing on the impact of frequency and boundary layer thickness on thermoacoustic oscillations. The initial conditions in the simulation also involve air at room temperature and stationary airflow. Therefore, according to the experiment, ΔT_{cri} under different $\omega\tau$ is obtained by using CFD, as depicted in Fig. 3(a). It can be observed that ΔT_{cri} obtained by CFD is decreased initially and then increased as $\omega\tau$ increases. The CFD results closely correspond with the experimental results for ΔT_{cri} but are slightly lower than. The largest discrepancy occurs at $\omega\tau = 0.46$, where the experimental ΔT_{cri} is approximately 14.91 % higher than the simulated values. This deviation is attributed to experimental factors such as gas leakage and heat loss due to sealing issues, which cause the experimental temperature gradient required for achieving self-excited oscillation in the looped TWTAE to be slightly higher than the CFD predictions under identical conditions [44]. Fig. 3(b) presents this frequency analysis, demonstrating that the experimental dominant frequency from Ref. [3] closely matches the fundamental mode frequency derived from CFD simulations (268.0 Hz vs. 271.4 Hz). This concordance verifies the effectiveness and accuracy of the CFD simulations when compared with experimental results, thus confirming the reliability of the looped TWTAE models we have established.

To verify the accuracy of the established Stirling TWTAE model, CFD simulation results are compared with the corresponding experimental data from Ref. [10]. According to the study by Wu et al. [10], the Stirling TWTAE oscillates in both high-frequency mode (HFM) and low-frequency mode (LFM). The HFM is associated with the oscillation of the looped tube, while the LFM corresponds to the oscillation of the resonator in the Stirling TWTAE. During the initial process, the Stirling TWTAE is mainly oscillated in the HFM before transitioning to the LFM. This phenomenon in the Stirling TWTAE is also observed in the previous experiments [45]. The spatial distribution of pressure amplitude for both modes of the Stirling TWTAE is obtained by FFT analysis and from the experimental data in Ref. [10], respectively, as depicted in Fig. 4(a).

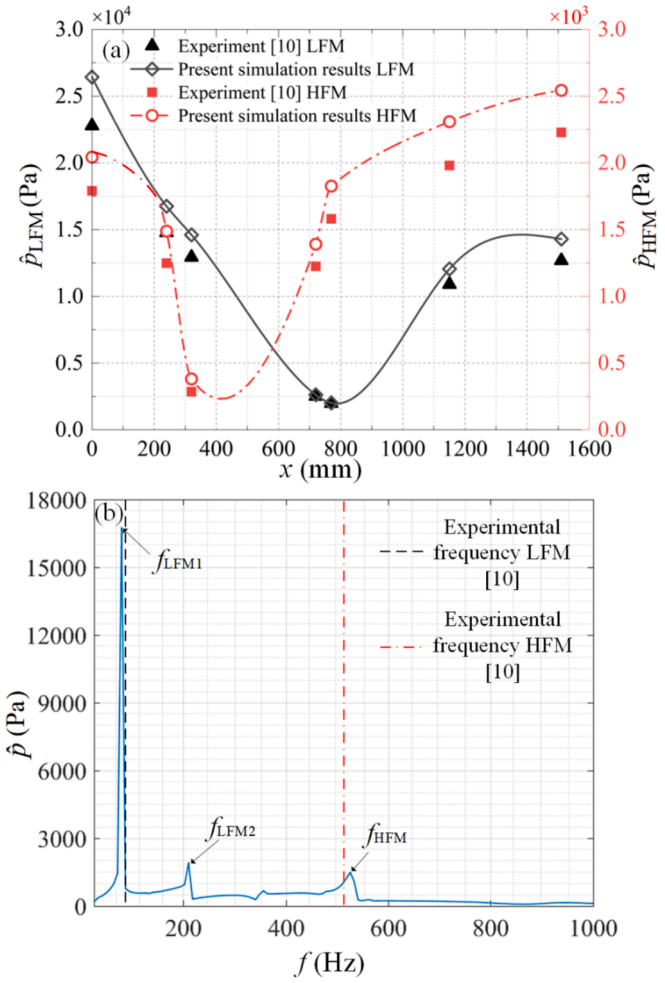

Fig. 4. Comparison of numerical and experimental results for (a) the spatial distribution of the pressure fluctuations at low-frequency mode (LFM) and high-frequency mode (HFM), and (b) frequency spectrum of the acoustic pressure fluctuations and the corresponding experimental frequency of the Stirling TWTAE.

The results indicate that HFM corresponds to a relatively low acoustic oscillations' amplitude, while LFM exhibits high acoustic amplitude. The trends of the pressure amplitude at low-frequency mode ($\hat{p}_{LFM}$) and high-frequency mode ($\hat{p}_{HFM}$) predicted by CFD are entirely consistent with the experimental results in Ref. [10]. In TAEs, the good agreement between experimental and simulation results in terms of pressure mode shapes implies similar acoustic fields between the simulation and experimental results. Furthermore, the CFD-predicted dominant low-frequency (f_{LFM}) and high-frequency (f_{HFM}) modes closely match the corresponding experimental results, as shown in Fig. 4(b). This consistency confirms the credibility of the Stirling TWTAE model and demonstrates the reliability of the CFD approach used in this study for evaluating the comprehensive performance of the Stirling TWTAE.

3. Comparison of the acoustic oscillation characteristics and inside flow fields among different types of thermoacoustic engines

3.1. Numerical models of different types of TAEs

To comprehensively compare the overall performances of the Stirling TWTAE and looped TWTAE, adjustments are made to the models established in Fig. 1, as depicted in Fig. 5 (a) and (b). The mean length of the looped TWTAE is approximately 1800 mm, with a constant inner diameter (D_l) of 21 mm. The regenerator is 30 mm long and consists of ten parallel solid plates, each with a thickness (t_{ls}) and plate spacing (t_{lp}) of 1 mm. The linear temperature gradient is imposed on the regenerator, ranging from the hot temperature at the left end ($T_h = 700$ K) to the cold temperature at the right end ($T_c = 300$ K), defined using User Defined Functions (UDF) [46]. The working medium/gas is air at a temperature of 300 K and an average atmospheric pressure of 101,325 Pa. To ensure consistency and facilitate comparison in the subsequent simulations, the mean length, inner diameter and regenerator parameters of the Stirling TWTAE are set identical to those of the looped TWTAE model, as shown in Fig. 5(b). Additionally, a full-scale SWTAE model with the same geometric dimensions is also established, as shown in Fig. 5(c).

3.2. The acoustic power output characteristics and thermo-acoustic energy efficiency of the different types of thermoacoustic engines

The self-excited thermoacoustic oscillations occur after a short period of energy accumulation in the three different TAE systems. During the initial process, the oscillations' pressure amplitude $|p_A'|$ is increased exponentially before reaching the 'saturation' state (i.e. limit cycle) in the thermoacoustic engines. The growth rate δ_g of the three different types of TAEs is obtained from the oscillations' growth rate function $F(t) = |p_a|e^{\delta_g t}$. The function $F(t)$ and the growth stages of the three engines are shown in Fig. 6(a). The data in Fig. 6(a) is obtained at the cold end side of the stack (regenerator). Table 2 presents the growth rate (δ_g), dominant oscillation frequency (f_{Rd}) during the initial process, and the time required to reach the saturation state (t) for the three TAEs. It can be seen that δ_g of the Stirling TWTAE is the lowest, and it takes the longest time to reach saturation. The SWTAE shows the highest δ_g and requires the least time to reach saturation ($t = 0.34$ s).

Following the initial process, limit cycle oscillations occur in all three TAE systems. The mode shapes of the limit cycle oscillations' acoustic pressure amplitude ($|p_A'|$) are shown in Fig. 6(b). It can be seen that $|p_A'|$ of the Stirling TWTAE is the largest, followed by the looped TWTAE, with that of the SWTAE is the smallest. Specifically, $|p_A'|$ of the Stirling and looped TWTAEs are 112.56 % and 54.40 % larger than that of the SWTAE, respectively. Meanwhile, the Stirling TWTAE exhibits the lowest frequency (115.50 Hz), followed by the looped TWTAE (126.56 Hz) and the SWTAE (151.00 Hz).

Furthermore, thermo-acoustic energy conversion efficiency (η) of the regenerator quantifies the efficiency of converting heat into acoustic energy, which can be calculated as

$$\eta = \frac{|\Delta I(\omega)|}{\dot{Q}_{in} + \dot{E}_f} \approx \frac{|\Delta \widehat{I}_{1A}(\omega)|}{\dot{Q}_{in} + \dot{E}_f} \tag{6}$$

where $\dot{Q}_{in}$ is the input heat power, and $\dot{E}_f$ is the forcing power of the external velocity perturbations (if present). Since the geometrical dimensions and temperature gradients of the regenerator (stack) are the same, the input heat for the three TAEs is also identical. Fig. 6(c) illustrates the fundamental-mode acoustic power generated by the regenerator (stack) ($\Delta \widehat{I}_{1A}(\omega)$) and thermo-acoustic energy conversion efficiency (η) for the three studied TAE models. The Stirling TWTAE generates the highest acoustic power (12.41 W), surpassing the looped TWTAE and SWTAE by 49.34 % and 364.79 %, respectively. The maximum efficiency ($\eta = 19.05\%$) is obtained in the Stirling TWTAE, while η of the SWTAE is 4.10 %. This difference can be attributed to the acoustic power of the TAE being primarily influenced by values of $|p_A'|$, $|v_A'|$ and the phase difference between them (θ). Fig. 7 presents a comparative analysis of the phase differences between the acoustic oscillation's velocity and pressure for the three thermoacoustic engines. The SWTAE exhibits the largest phase difference, suggesting a higher component of standing waves within its acoustic fields. This substantial phase difference, approaching 90 degrees, corresponds to minimal acoustic power generation. Consequently, the SWTAE demonstrates the

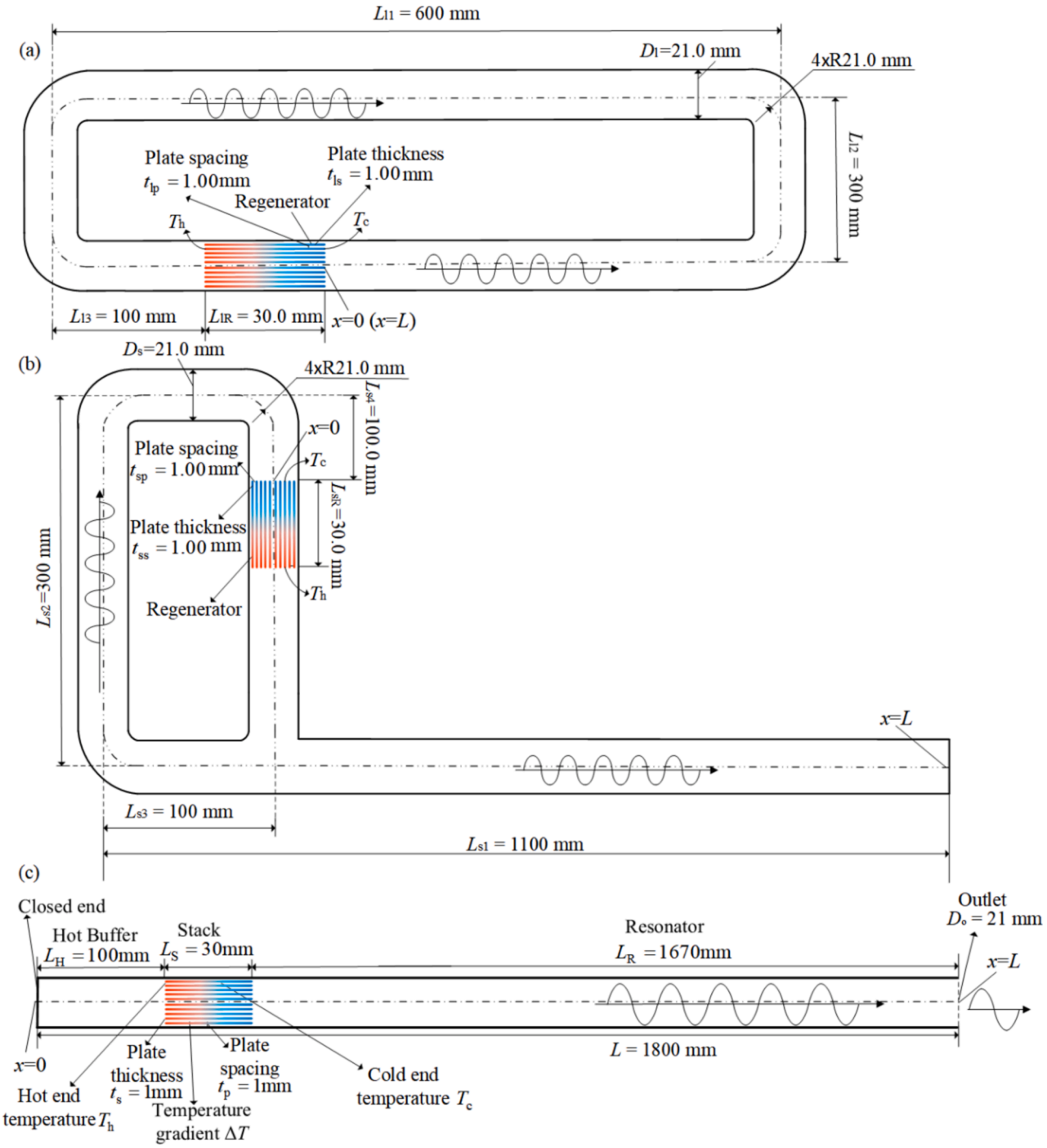

Fig. 5. 2D full-scale numerical model of the (a) looped TWTAE, (b) Stirling TWTAE, and (c) SWTAE, with the same geometric dimensions.

lowest acoustic power output and thermo-acoustic energy conversion efficiency among the studied models. Conversely, the Stirling TWTAE shows the smallest phase difference, signifying a predominant presence of traveling waves in its acoustic fields. From the thermodynamics perspective, the traveling wave thermoacoustic engine is characterized by near-isothermal compression and expansion processes, which enable more effective heat exchange between the oscillating gas and the solid wall. This efficient thermal interaction enhances the thermal-acoustic energy conversion of the system, thereby improving the overall acoustic power output and energy conversion efficiency.

In summary, although the SWTAE has a simpler structure and a higher initial growth rate, leading to a quicker saturation state, its overall performance in terms of acoustic power and efficiency is inferior to the other models. Under identical geometric parameters and operating conditions, the Stirling TWTAE outperforms the other models in terms of acoustic characteristics and thermo-acoustic energy conversion efficiency.

3.3. *Instantaneous velocity characteristics of different types of TAEs*

The heat-driven flow fields in different types of TAEs are presented in this section [47,48]. Phases φ_1 to φ_4 are selected at intervals of a quarter period over a complete acoustic cycle to display the flow fields. Phases φ_2 and φ_4 represent the moments when the velocity reaches its maximum, referred to as velocity anti-nodes, while φ_1 and φ_3 correspond to the velocity nodes. For comparison, the TAE models are

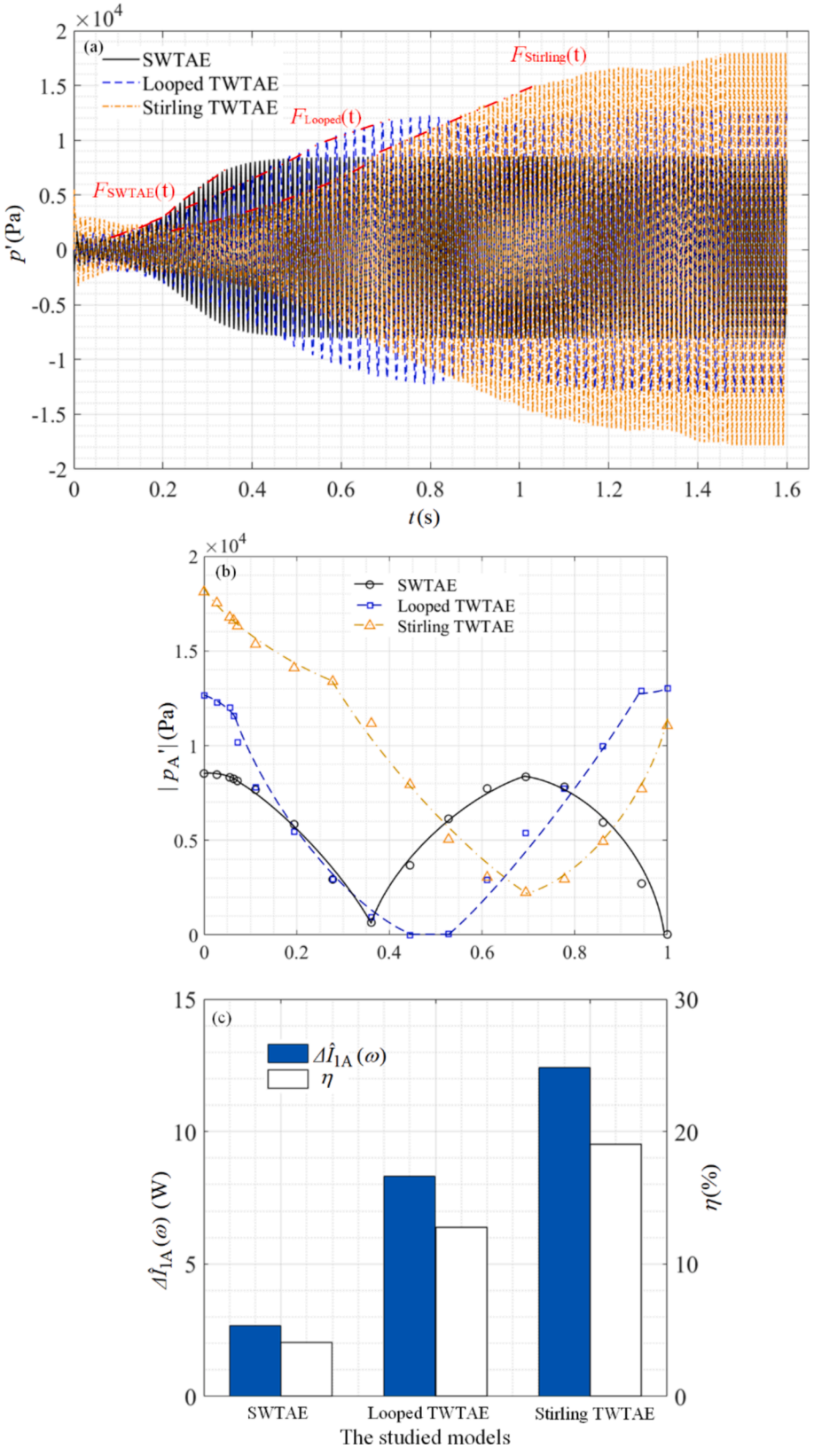

Fig. 6. Comparison of (a) the oscillations' growth rate functions with growth stages, (b) the mode shapes of the limit cycle oscillations' acoustic pressure amplitudes, and (c) fundamental-mode acoustic power generated by the regenerator (stack) and thermo-to-acoustic efficiency of the SWTAE, looped TWTAE and Stirling TWTAE models, respectively.

Table 2
A comparison of the oscillations' growth rate, dominant mode frequency and time required to reach saturation of the three different types of TAEs.

	SWTAE	Looped TWTAE	Stirling TWTAE
δ_g	15.34	8.89	5.10
f_{Rd} (Hz)	153.44	128.81	425.10
Time required to reach saturation t (s)	0.34	0.81	1.47

analyzed at phases φ_2 and φ_4, where the self-excited thermoacoustic oscillations' velocity reaches its maximum, as illustrated in Fig. 8. The velocity vectors in Fig. 8 (a), (c), and (e) indicate that, at phase φ_2, the working gas/medium predominantly flows from the hot-end side to the cold-end side of the stack/regenerator. Conversely, at phase φ_4, the flow direction reverses, moving from the cold-end side to the hot-end side, as illustrated in Fig. 8 (b), (d), and (f). The color representing the maximum velocity region of the SWTAE in Fig. 8(e) and (f) is darker compared to that of the Stirling TWTAE in Fig. 8(a) and (b), and the looed TWTAE in Fig. 8(c) and (d). This implies that the SWTAE has the largest amplitude of self-excited thermoacoustic oscillations' velocity among the three studied TAE models. According to the previous research [11,49], the

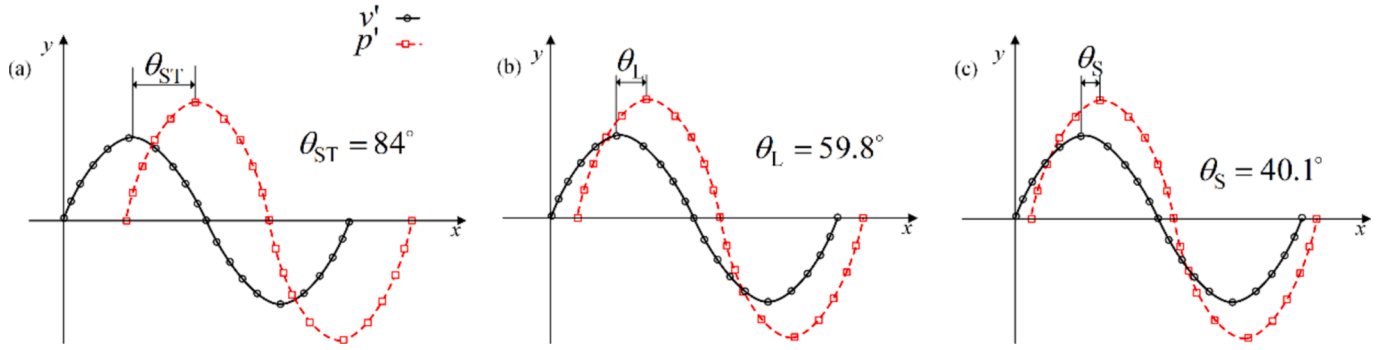

Fig. 7. The phase difference of acoustic oscillations' velocity leading pressure in (a) SWTAE, (b) looped TWTAE, and (c) Stirling TWTAE.

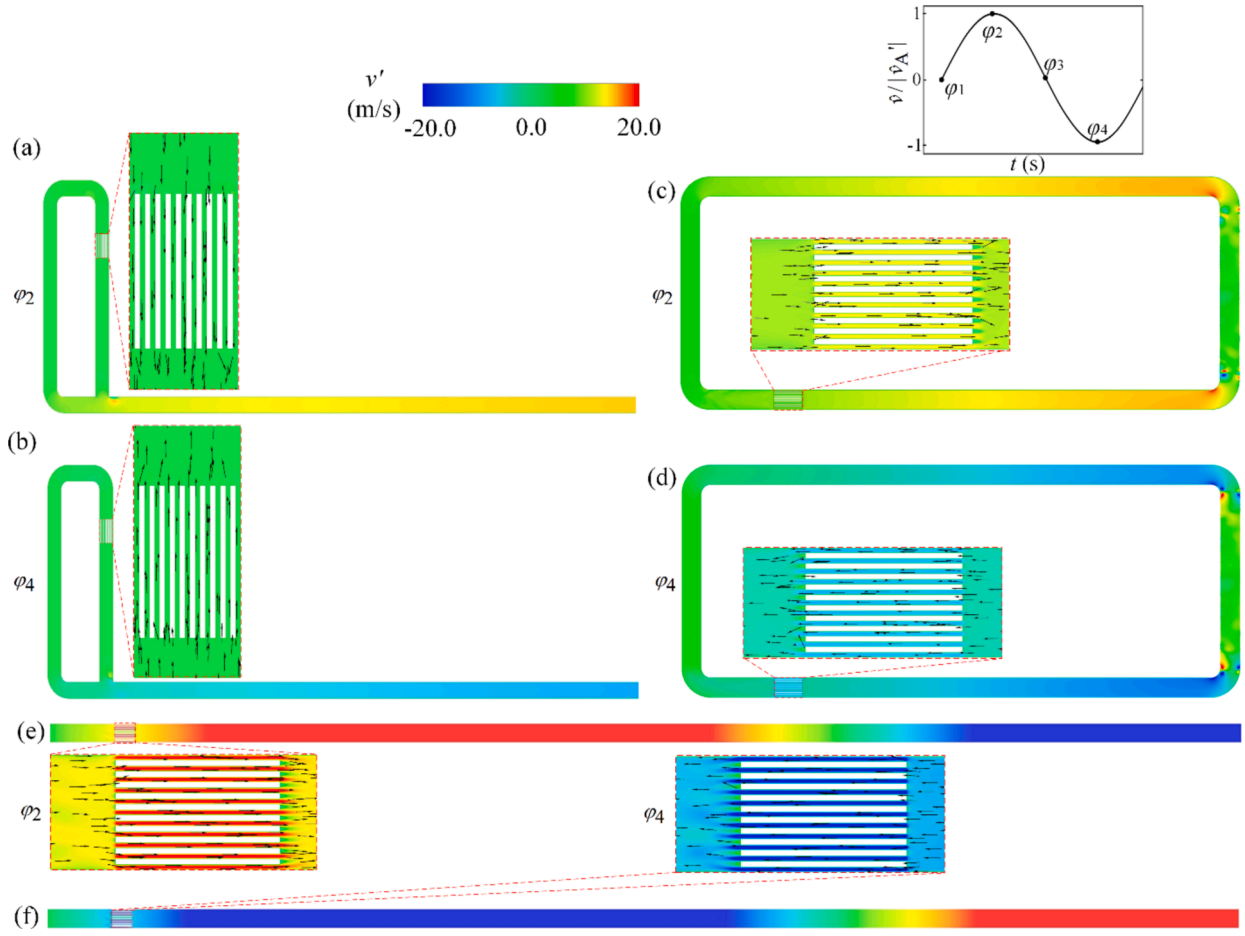

Fig. 8. The instantaneous flow velocity contours of the thermoacoustic engines at velocity anti-nodes, (a) Stirling TWTAE at φ_2, (b) Stirling TWTAE at φ_4, (c) looped TWTAE at φ_2, (d) looped TWTAE at φ_4, (e) SWTAE at φ_2, and (f) SWTAE at φ_4.

term $v\frac{\partial v}{\partial x}$ represents the nonlinear component, which increases sharply as oscillation characteristics intensify. This increase triggers a series of bifurcations in the steady-state dynamics, allowing the system to access additional modes that were previously less prominent or inactive at lower amplitudes. As a result, higher harmonics are excited, leading to mode transitions [50,51]. The self-excited thermoacoustic oscillations' velocity of the Stirling TWTAE is the smallest, indicating a minimal nonlinear term $v\frac{\partial v}{\partial x}$. This is also one reason why the Stirling SWTAE achieves the highest output power and thermal efficiency.

4. Thermodynamic characteristics and nonlinear dynamics phenomena of the Stirling TWTAE

Since the Stirling TWTAE exhibits the optimal acoustic characteristics among the three types of thermoacoustic devices, this section further explores the simulation efforts of the Stirling TWTAE under varied operational conditions to elucidate its corresponding acoustic oscillation characteristics and nonlinear behaviors.

4.1. Bistability of the Stirling TWTAE with different temperature gradient paths

When the temperature gradient along the regenerator surpasses the critical value (onset temperature ΔT_{cri}), the thermoacoustic engine undergoes a mode transition from a stationary state to a periodically oscillating state. ΔT_{cri} can be roughly estimated through linear theory [52,53]. However, the mode transition process is susceptible to nonlinear phenomena, such as bistablity, which has been observed in the SWTAE through CFD simulations in previous research [54]. To investigate the onset characteristics of the Stirling TWTAE in relation to variations in the temperature gradient, simulations are conducted along two distinct paths. The cold-end temperature (T_c) of the Stirling TWTAE remains constant at 300 K, while the hot-end temperature (T_h) is varied systematically through reverse (decreasing T_h from 505 K to 385 K) and forward (increasing T_h from 390 K to 510 K) paths. Fig. 9(a) illustrates the resulting self-excited oscillation pressure amplitude ($|p_A'|$) under the continuously changing temperature gradient of the regenerator. It can be seen in Fig. 9(a) that when T_h of the system is below T_{h1}, $|p_A'|$ is 0 for both forward and reverse paths, indicating that no thermal oscillations occur within the system. The onset characteristics of the Stirling TAE exhibit a sudden process in the forward path. When T_h of the system exceeds 456 K, limit cycle oscillations suddenly occur. On the other hand, in the reverse path (damping process), the reduction of $|p_A'|$ is gradual as T_h is reduced, reaching a stationary state at T_{h1}. When T_h is between T_{h1} (410 K) and T_{h2} (485 K), the curves for the forward and reverse paths form a bistable/two-valued zone, known as a 'hysteresis loop'. Within this zone, the Stirling TWTAE can exhibit either limit cycle oscillations or remain steady. T_{h1} and T_{h2} are defined as the two critical bistability values. When T_h of the system is above T_{h2}, $|p_A'|$ values remain consistent during both the forward and reverse paths, increasing linearly with T_h. The time histories of acoustic pressure oscillations (p') for four selected temperatures are depicted through the reverse and forward paths in Fig. 9(b) and (c), respectively. Time zero is defined as the moment when the temperature gradient is applied to the regenerator of the Stirling engine, marking the start of the simulation. Fig. 9(b) demonstrates that along the reverse path, the system maintains limit cycle oscillations at $T_h = 411$ K, and reaching to the steady state at $T_h = 409$ K. In contrast, along the forward path, shown in Fig. 9(c), the system remains in a steady state even when T_h reaching 456 K, with self-excited oscillations occurring only at $T_h = 458$ K.

This phenomenon can be interpreted from a nonlinear dynamic perspective [55]. Bistability occurs when the system transitions between two stable states. The state of the system depends not just on the current conditions but also on its historical state, effectively functioning as a memory of its past [56]. In the forward path, the system remains in a non-oscillatory state, and the temperature must exceed the critical threshold, triggering limit cycle oscillations and causing a sudden change. On the backward path, since the system has been in a limit cycle oscillation state, it effectively acts as if external disturbances were applied, thus maintaining the limit cycle oscillation until the temperature drops below T_{h1}, leading the system to become stationary. This explains why the forward path exhibits a sudden transition, while the backward path shows a gradual decline.

4.2. Effect of the inlet disturbance on the acoustic oscillation characteristics of the Stirling TWTAE

The impact of forcing periodic perturbations on the nonlinear phenomena and thermal-acoustic conversion efficiency of the Stirling TWTAE is examined. An externally applied forcing disturbance is introduced at the resonator right end of the engine, designated as the pressure/velocity inlet. Numerical simulations are conducted under varying forced frequencies (f_f) ranging from 0.1 Hz to 600 Hz, and amplitudes of pressure (p_f) set at 50 Pa or 100 Pa, or velocity (v_f) ranging from 1 m/s to 10 m/s perturbations on the Stirling TWTAE. The absolute

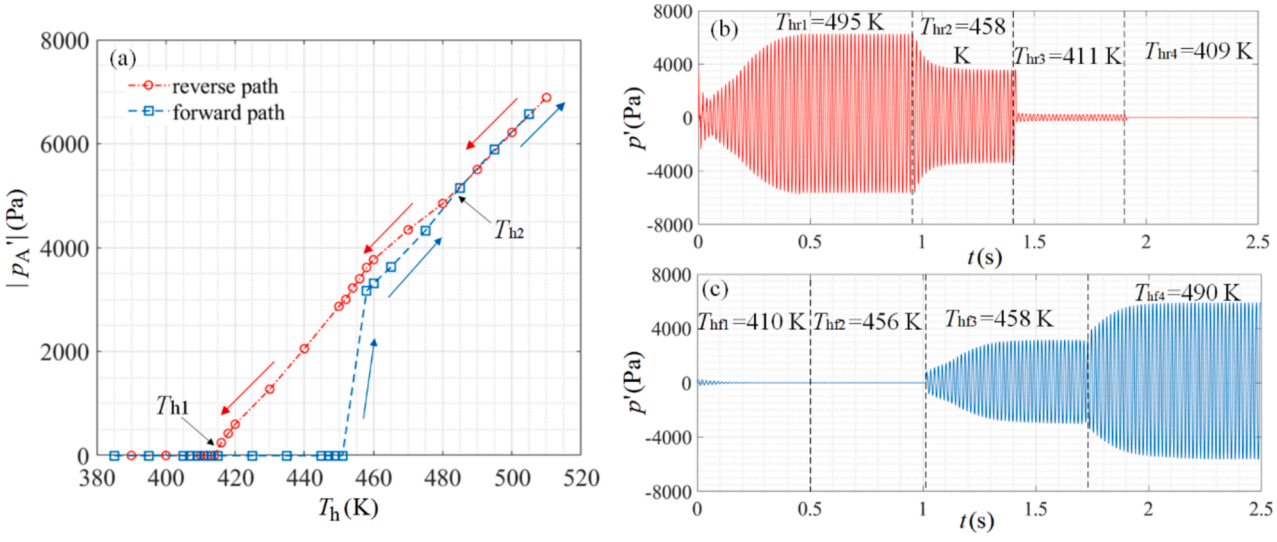

Fig. 9. (a) Bistability in the oscillation pressure amplitude of the Stirling TWTAE induced by variations in the hot-end temperature through forward and reverse paths, and the time histories of acoustic pressure oscillations at different temperatures in the (b) reverse path and (c) forward path.

values of pressure amplitude of the oscillation ($|p_A'|$) under different forced perturbations are shown in Fig. 10(a). The mode transition phenomenon in the pressure oscillations of the Stirling TWTAE is observed:

(1) In the presence of forced pressure p_f, $|p_A'|$ is remained at 0 across different forced frequencies f_f, 'damping' in the Stirling TWTAE system [57]. The damping also occurs when forced velocity v_f is applied. As f_f approaches 0 Hz, self-excited oscillations are damped, creating a steady region (S).
(2) As f_f increases, the quasi-periodic oscillation area (QP1) is observed, arising from the combined influence of f_f and the Stirling TAE's self-excited oscillation frequency (f_s = 115 Hz), leading to non-fixed frequency oscillations [58,59].
(3) When f_f is close to f_s, a limit cycle oscillation is observed (LM1). This occurs due to constructive interference, where the resonance between the forced frequency and the system's self-excited fundamental mode causes similar frequencies to reinforce each other, increasing the overall pressure amplitude [60].
(4) When f_f exceeds 150 Hz, the resonance condition is disrupted, and f_f coexists with f_s without interference, leading to quasi-periodic behavior (QP2 and QP3 regions). In this scenario, the energy conversion of the self-excited thermoacoustic oscillation remains similar to that of the unforced system, and the system response amplitude barely changes, leveling off.
(5) When f_f approaches the second harmonic frequency of the Stirling TWTAE (230 Hz), the system enters another limit cycle state (LM2). However, since the pressure amplitude corresponding to

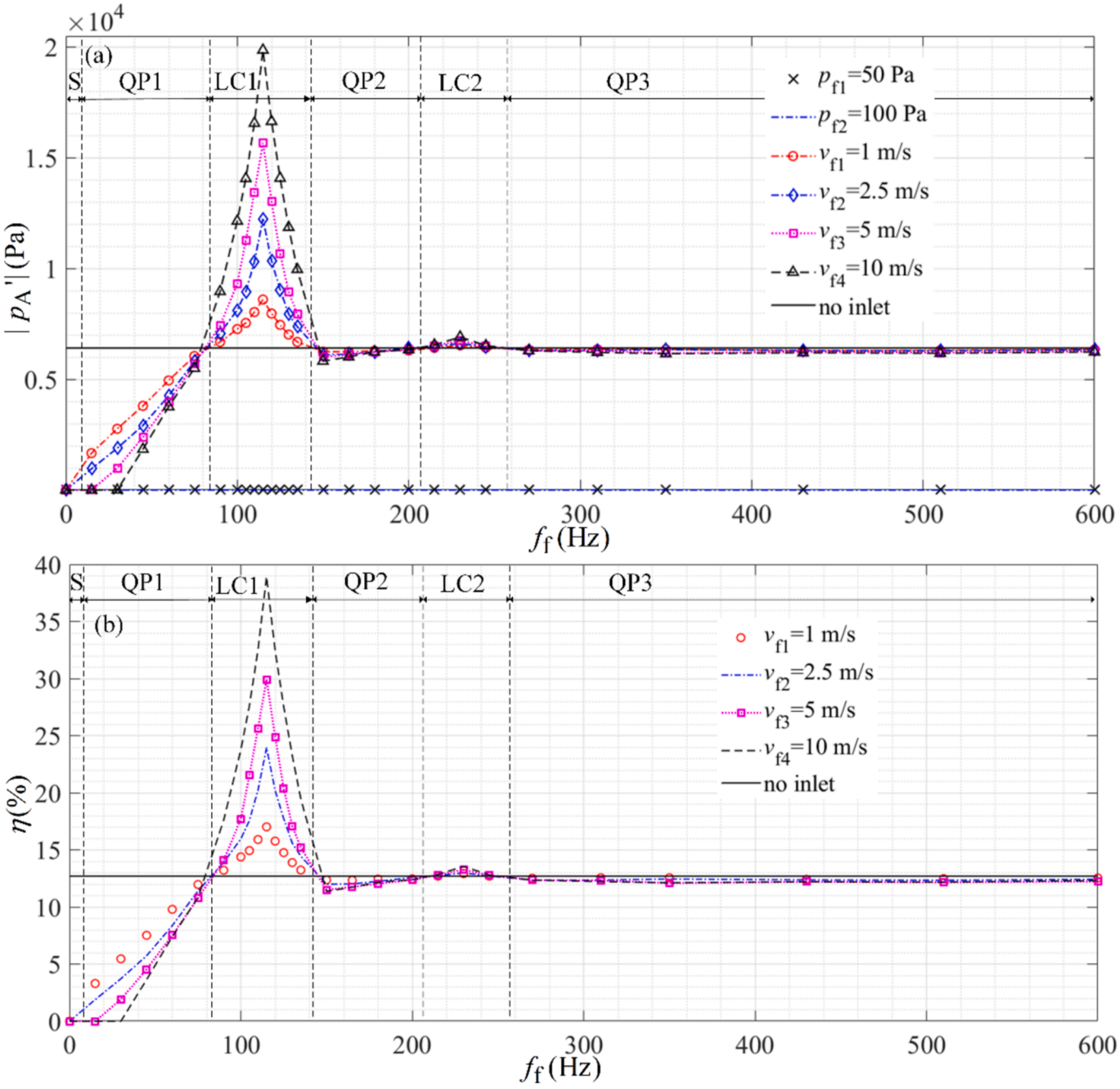

Fig. 10. Effect of the forcing pressure/velocity perturbations on the (a) oscillations' acoustic pressure amplitude and (b) thermal-acoustic conversion efficiency of the Stirling TWTAE, with the no inlet corresponds to the relevant values of the unforced TAE model.

the second harmonic is inherently small, even resonance with the forcing disturbance does not significantly impact the overall pressure amplitude, resulting in only a slight increase in $|p_A'|$.

This is consistent with our previous findings on the SWTAE with external forcing perturbations [54], where a more detailed explanation of mode transitions is provided in the paper. To further investigate the impact of forcing periodic perturbations on the thermo-acoustic conversion efficiency of the Stirling TWTAE, the thermal efficiency of the forced system (η) is calculated by Eq. (6), as shown in Fig. 10(b). It is observed η notably increases when f_f lies between 90 Hz and 135 Hz, equivalent to $0.78 < f_f/f_s < 1.17$. The influence of f_f on η intensifies with elevated forced velocity amplitudes. The highest thermal efficiency of 38.93 % occurs at a forced velocity of 10 m/s at 115 Hz, markedly surpassing the system's efficiency without inlet forcing, which stands at 12.70 %. Therefore, providing the Stirling TWTAE system with a forced frequency close to its self-excited frequency ($0.78 < f_f/f_s < 1.17$) and a high amplitude is a beneficial trade-off, as it enhances both the acoustic oscillation characteristics and thermo-acoustic energy conversion efficiency.

4.3. Mass streaming

Mass streaming, characterized by the time-averaged second harmonic mass flow superimposed on the fundamental limit cycle oscillation mode, significantly influences the acoustic performance of thermoacoustic devices [61]. Specifically, Gedeon streaming arises from the imbalance between positive and negative flows in each half cycle, resulting in a net mass flow [62,63]. To identify this phenomenon, the time-averaged air mass flow rate ($\overline{\rho v}$) is calculated. As illustrated in Fig. 11(a), the primary direction of $\overline{\rho v}$ circulates from the hot side of the regenerator, through the looped tube, and reaches the ambient side of the regenerator. At a regenerator hot-end temperature of 900 K, a distinct variation in $\overline{\rho v}$ is observed, transitioning from blue (indicating high mass flux downward) to red (indicating high mass flux forward), particularly in the regenerator area and at the junction between the loop tube and the resonator tube, where significant mass flux is observed. Fig. 11(b) (700 K) exhibits a similar pattern but with reduced overall flux, suggesting a reduction in the mass flux at lower hot-end temperatures. In Fig. 11(c) (500 K), $\overline{\rho v}$ is further decreased, with almost no red areas in the tube, demonstrating a significant reduction in the second harmonic velocity at 500 K. This occurs because temperature gradients in thermoacoustic devices lead to thermal expansion and compression of the gas, generating pressure gradients that drive fluid flow, resulting in Gedeon streaming. As the temperature difference is increased, so do the resulting density and pressure differentials, making Gedeon streaming more pronounced with increasing temperature gradients.

To further quantitatively compare the time-averaged mass flux ($\overline{\rho v}$) at different positions within the engine under various regenerator hot-end temperatures, eight points (x_1, x_2, x_3, x_4, x_5, x_6, x_7, and x_8) are selected within the engine. Radial profiles of $\overline{\rho v}$ at these points under different hot-end temperatures (900 K, 700 K, 500 K) are obtained, as shown in Fig. 12. Significant fluctuations in $\overline{\rho v}$ are observed at positions x_1, x_3, and x_5 (see Fig. 12 (a), (c), and (e)), indicating higher mass flux and pronounced nonlinear effects in these regions. In the resonator tube, a comparison of positions x_6, x_7, and x_8 (see Fig. 12 (f), (g), and (h)) reveals that $\overline{\rho v}$ is decreased with increasing distance from the looped tube, reflecting the attenuation characteristics of $\overline{\rho v}$ with distance from the looped tube. Moreover, at the regenerator hot-end temperature of 900 K, $\overline{\rho v}$ is the highest at nearly all positions (i.e., x_1 to x_8) compared to

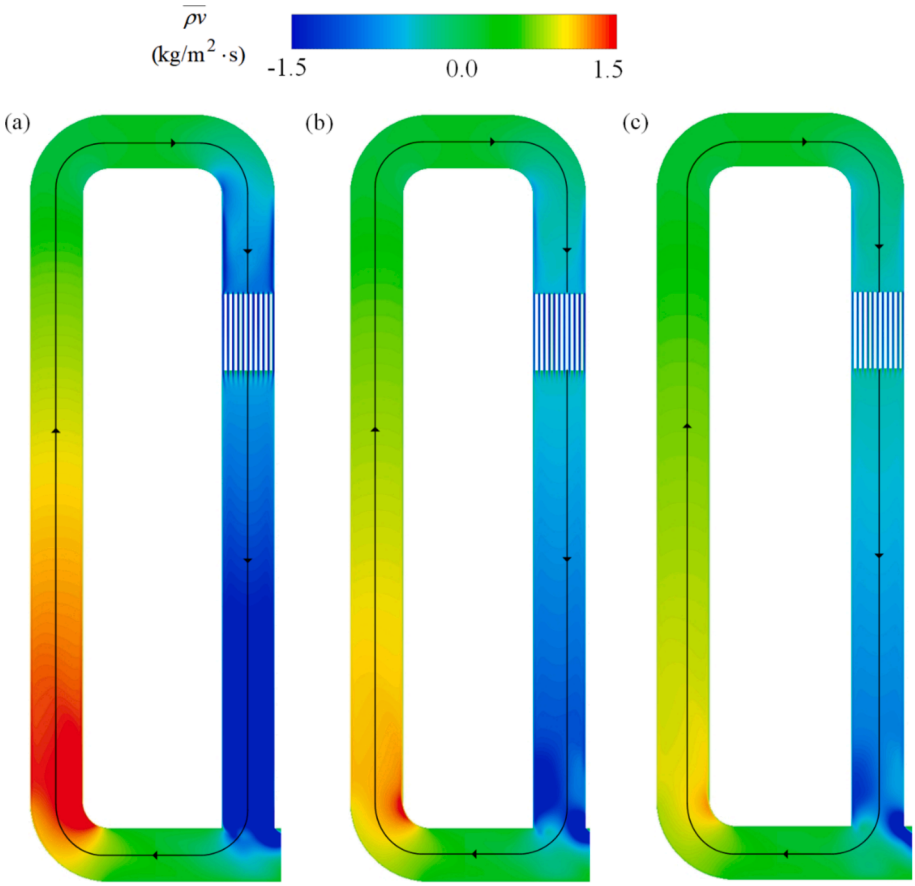

Fig. 11. Comparison of the time-averaged mass flux $\overline{\rho v}$ in the looped tube of the Stirling TWTAE at regenerator hot-end temperatures of (a) 900 K, (b) 700 K, and (c) 500 K.

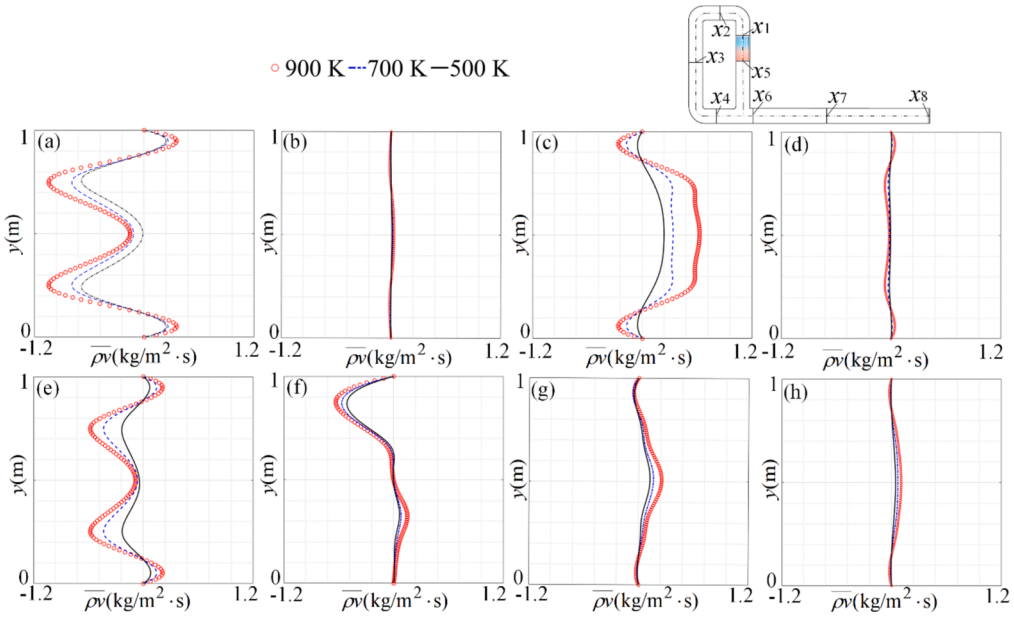

Fig. 12. Comparison of radial profiles of the time-averaged mass flux $\overline{\rho v}$ at selected axial positions (a) x_1, (b) x_2, (c) x_3, (d) x_4, (e) x_5, and (d) x_6 of the Stirling TWTAE under different hot-end temperatures of 900 K, 700 K, and 500 K.

those at lower regenerator hot-end temperatures (500 K and 700 K). This trend underscores the significant impact of temperature gradients on the nonlinear characteristics of mass flux.

Additionally, Fig. 12 shows that reverse $\overline{\rho v}$ near the tube walls is observed at axial positions x_1 to x_8 across all temperature settings in the Stirling TWTAE. This phenomenon, known as Rayleigh streaming, is induced by boundary-layer effects along the engine walls [64–66]. Rayleigh streaming is another significant type of mass streaming that affects thermoacoustic phenomena and flow fields in thermoacoustic engines. It can lead to alterations in the flow fields near the tube walls, changing the phase and amplitude of sound waves, reducing the effective transfer of thermal energy, and potentially decreasing system efficiency. Fig. 12 also demonstrates that as the regenerator hot-end temperature decreases, the intensity of Rayleigh streaming correspondingly weakens. In summary, a detailed view of the radial and axial distribution of mass flux in the Stirling TWTAE under different temperatures is provided, revealing the influence of temperature and boundary-layer effects on mass flux in thermoacoustic engines. The comparisons lead to the conclusion that appropriately reducing the regenerator's hot-end temperature can mitigate mass streaming.

5. Discussion and conclusions

In this study, comprehensive numerical simulations using Computational Fluid Dynamics (CFD) are conducted on full-scale looped traveling-wave thermoacoustic engines (TWTAEs) and Stirling TWTAEs to explore their overall performance and nonlinear effects. The primary objectives are to 1) establish and validate full-scale numerical TWTAE models, 2) compare different types of thermoacoustic engines under identical operating conditions, and 3) investigate the nonlinear effects in the Stirling TWTAE. The key contributions of this work are outlined as follows:

- Development and validation of full-scale time-domain models: This study establishes full-scale, two- and three-dimensional (2D and 3D) time-domain numerical models for both looped and Stirling TWTAEs. These models are validated by assessing the impact of different turbulence models on simulation results and through comparisons with experimental data available in the literature. Time-efficient and accurate full-scale 2D models for both looped and Stirling TWTAEs are identified, demonstrating their capability to capture the acoustic oscillation characteristics and heat transfer properties of these engines.
- Comparative analysis of traveling-wave thermoacoustic systems: 2D models of looped TWTAE, Stirling TWTAE, and standing-wave thermoacoustic engines are developed with identical geometrical parameters, and their performances are comprehensively compared under the same operating conditions. The comparative analysis of the acoustic characteristics and flow fields of the different thermoacoustic engines reveal that the Stirling TWTAE outperforms the other systems in terms of heat-driven acoustic power and thermoacoustic energy conversion efficiency. This is attributed to the minimal nonlinear phenomena within the flow fields and the small phase differences between acoustic velocity and pressure oscillations, which enhance the overall heat-to sound energy conversion process.
- Exploration of nonlinear dynamics phenomena of the Stirling TWTAE: This present study delves into the nonlinear dynamics of the flow fields within the Stirling TWTAE, demonstrating how operational parameters, such as temperature gradients across the regenerator, can be adjusted to control bistability phenomena and to manage mass streaming effects, including Gedeon and Rayleigh streaming. Further investigations reveal that enhancing the Stirling TWTAE's performance can be achieved by introducing forcing frequency perturbations closely aligned with the engine's self-excited oscillations frequency, particularly when combined with large forced amplitudes.

In general, this present work demonstrates the reliability and robustness of time-domain CFD models in predicting acoustic oscillation characteristics and exploring nonlinear dynamics phenomena in the heat-driven flow fields of full-scale TWTAEs. These interesting findings provide physical insights into the distinct characteristics and operational advantages of the Stirling TWTAE, highlighting its potential as a highly efficient thermoacoustic engine for energy conversion. These insights lay a foundation for future developments, optimizations, and analysis of traveling-wave thermoacoustic systems. However, the startup and stability of heat-driven acoustic oscillations in the design of Stirling TWTAE dynamics are important aspects that certainly attract more attention, and these will be included in our future research.

Declaration of competing interest

The authors declare that they have no known competing financial interests or personal relationships that could have appeared to influence the work reported in this paper.

Acknowledgments

We would like to acknowledge the financial support (452DISDZ) from the University of Canterbury, New Zealand. The first author would like to thank the University of Canterbury for providing Ph.D. scholarship. Dakun Sun would like to acknowledge the financial support from the project funded by Science Center for Gas Turbine Project (P2022-C-II-003-001). Yue Zhang would like to acknowledge the financial support from the project funded by Science Center for Gas Turbine Project (P2022-C-II-002-001).

Data Availability.

The data that support the findings of this study are available from the corresponding authors upon reasonable request.

Data availability

Data will be made available on request.

References

[1] J. Huang, R. Yang, Y. Yang, Q. Zhou, E. Luo, Generalized thermoacoustic heat engines with unconventional working substances: A review, Appl. Energy 347 (2023) 121447.
[2] G.W. Swift, Thermoacoustics: A unifying perspective for some engines and refrigerators, J. Acoust. Soc. Am. (2003).
[3] T. Yazaki, A. Iwata, T. Maekawa, A. Tominaga, Traveling wave thermoacoustic engine in a looped tube, Phys. Rev. Lett. 81 (15) (1998) 3128.
[4] S. Zare, A. Tavakolpour-Saleh, A. Aghahosseini, R. Mirshekari, Thermoacoustic Stirling engines: A review, Int. J. Green Energy 20 (1) (2023) 89–111.
[5] L. Guo, D. Zhao, S. Becker, Temperature difference and stack plate spacing effects on thermodynamic performances of standing-wave thermoacoustic engines driven by cryogenic liquids and waste heat, J. Therm. Sci. 31 (5) (2022) 1434–1451.
[6] Z. Wu, W. Dai, M. Man, E. Luo, A solar-powered traveling-wave thermoacoustic electricity generator, Sol. Energy 86 (9) (2012) 2376–2382.
[7] G. Chen, S. Tao, R. Liang, Z. Li, W. Sun, J. Xu, Z. Yu, Development of a sunlight-driven thermoacoustic engine for solar energy harvesting, Appl. Therm. Eng. 238 (2024) 122047.
[8] Z. Yu, A. Al-Kayiem, Numerical analysis of a thermally driven thermoacoustic heat pump for low-grade heat recovery, Comput. Therm. Sci.: Int. J. 6 (4) (2014).
[9] H. Kang, G. Zhou, Q. Li, Heat driven thermoacoustic cooler based on traveling–standing wave, Energy Convers. Manage. 51 (11) (2010) 2103–2108.
[10] J. Wu, Q. Li, F. Guo, Experimental investigation of self-sustained oscillation in a traveling wave thermoacoustic system, J. Therm. Sci. 12 (2003) 51–56.
[11] L. Guo, D. Zhao, Effects of temperature difference and operating pressures on heat-driven acoustic characteristics and nonlinear behaviors in a looped tube traveling wave thermoacoustic engine, J. Acoust. Soc. Am. 154 (4_supplement) (2023) A286–A.
[12] L. Xiao, K. Luo, D. Zhao, G. Chen, T. Bi, J. Xu, E. Luo, Time-domain acoustic-electrical analogy investigation on a high-power traveling-wave thermoacoustic electric generator, Energy 263 (2023) 126088.
[13] Z. Yu, A.J. Jaworski, Impact of acoustic impedance and flow resistance on the power output capacity of the regenerators in travelling-wave thermoacoustic engines, Energy Convers. Manage. 51 (2) (2010) 350–359.
[14] P.H. Ceperley, A pistonless Stirling engine—The traveling wave heat engine, J. Acoust. Soc. Am. 66 (5) (1979) 1508–1513.
[15] P.H. Ceperley, Gain and efficiency of a traveling wave heat engine, J. Acoust. Soc. Am. 72 (6) (1982) 1688–1694.
[16] S. Backhaus, G. Swift, A thermoacoustic Stirling heat engine, Nature 399 (6734) (1999) 335–338.
[17] D.L. Gardner, G. Swift, A cascade thermoacoustic engine, J. Acoust. Soc. Am. 114 (4) (2003) 1905–1919.
[18] G. Yu, E. Luo, W. Dai, Z. Wu, An energy-focused thermoacoustic-Stirling heat engine reaching a high pressure ratio above 1.40, Cryogenics 47 (2) (2007) 132–134.
[19] B. Yu, E. Luo, S. Li, W. Dai, Z. Wu, Experimental study of a thermoacoustically-driven traveling wave thermoacoustic refrigerator, Cryogenics 51 (1) (2011) 49–54.
[20] K. Luo, E. Luo, X. Xie, Y. Jiang, A highly efficient heat-driven thermoacoustic system for room-temperature refrigeration by using novel configuration, Appl. Energy 357 (2024) 122530.
[21] L. Xiao, K. Luo, Z. Wu, J. Chi, J. Xu, L. Zhang, J. Hu, E. Luo, A highly efficient heat-driven thermoacoustic cooling system, Cell Rep. Phys. Sci. 5 (2) (2024).
[22] S.H. Hsu, C.H. Lai, Evaluating the onset conditions of a thermoacoustic Stirling engine loaded with an audio loudspeaker, Front. Therm. Eng. 3 (2023) 1241411.
[23] S.H. Hsu, Z.Y. Liao, Impedance matching for investigating operational conditions in thermoacoustic Stirling fluidyne, Appl. Energy 374 (2024) 123973.
[24] S.H. Hsu, H.E. Lin, Condensation shock induced in wet thermoacoustic prime mover, Phys. Fluids 36 (5) (2024).
[25] S. Zare, A. Tavakolpour-Saleh, Design of a traveling wave thermo-acoustic engine based on genetic algorithm, Int. J. Energy Res. 43 (14) (2019) 8790–8801.
[26] S. Zare, A. Tavakolpour-Saleh, A. Hosseininia, M.H. Sangdani, Investigating the onset and steady-state conditions of a diaphragm thermoacoustic stirling engine, Proceedings of the Institution of Mechanical Engineers, Part a: Journal of Power and Energy 238 (4) (2024) 731–760.
[27] S. Zare, A. Tavakolpour-Saleh, Modeling, construction, and testing of a diaphragm thermoacoustic Stirling engine, Energy Convers. Manage. 243 (2021) 114394.
[28] L. Guo, D. Zhao, Enhancing heat-driven acoustic characteristics of standing wave thermoacoustic engines by using corrugated stack, J. Acoust. Soc. Am. 154 (4_supplement) (2023) A285–A286.
[29] A. Di Meglio, N. Massarotti, CFD modeling of thermoacoustic energy conversion: a review, Energies 15 (10) (2022) 3806.
[30] H.K. Versteeg, W. Malalasekera, An Introduction to Computational Fluid Dynamics: the Finite, volume method, Pearson Education, 2007.
[31] L. Guo, D. Zhao, G. Yu, X. Dong, Numerical investigations on energy conversion performances in twin standing-wave thermoacoustic engines with various geometric and operational conditions, Therm. Sci. Eng. Prog. 45 (2023) 102134.
[32] J. Lycklama, à. Nijeholt, M. Tijani, S. Spoelstra, Simulation of a traveling-wave thermoacoustic engine using computational fluid dynamics, J. Acoust. Soc. Am. 118 (4) (2005) 2265–2270.
[33] J.L.A. Nijeholt, M. Tijani, S. Spoelstra, M. Loginov, A. Kuczaj, CFD modeling of streaming phenomena in a torus-shaped thermoacoustic engine, in, in: Proceedings of the 19th International Congress on Sound and Vibration, 2012, pp. 1–8.
[34] P. Yang, H. Chen, Y. Liu, Numerical investigation on nonlinear effect and vortex formation of oscillatory flow throughout a short tube in a thermoacoustic Stirling engine, J. Appl. Phys. 121 (21) (2017).
[35] G. Yu, E. Luo, W. Dai, J. Hu, Study of nonlinear processes of a large experimental thermoacoustic-Stirling heat engine by using computational fluid dynamics, J. Appl. Phys. 102 (7) (2007).
[36] E.M. Sharify, S. Takahashi, S. Hasegawa, Development of a CFD model for simulation of a traveling-wave thermoacoustic engine using an impedance matching boundary condition, Appl. Therm. Eng. 107 (2016) 1026–1035.
[37] S. Shanmuganathan, D. Youngs, J. Griffond, B. Thornber, R. Williams, Accuracy of high-order density-based compressible methods in low Mach vortical flows, Int. J. Numer. Methods Fluids 74 (5) (2014) 335–358.
[38] A. Moradi, D. Toghraie, A.H.M. Isfahani, A. Hosseinian, An experimental study on MWCNT–water nanofluids flow and heat transfer in double-pipe heat exchanger using porous media, J. Therm. Anal. Calorim. 137 (5) (2019) 1797–1807.
[39] J.M. Huang, W.C. Hsieh, X.J. Ke, C.C. Wang, The effects of frost thickness on the heat transfer of finned tube heat exchanger subject to the combined influence of fan types, Appl. Therm. Eng. 28 (7) (2008) 728–737.
[40] A.B. Zarch, K. Mazaheri, A numerical investigation on stack sides thermo-gas dynamic in a large amplitude standing wave thermoacoustic engine, Appl. Therm. Eng. 234 (2023) 121288.
[41] M. McGaughy, C. Wang, E. Boessneck, T. Salem, J. Wagner, A traveling wave thermoacoustic engine—design and test, ASME Lett. Dyn. Syst. Control 1 (3) (2021) 031006.
[42] T. Bi, Z. Wu, W. Chen, L. Zhang, E. Luo, B. Zhang, Numerical and experimental research on a high-power 4-stage looped travelling-wave thermoacoustic electric generator, Energy 239 (2022) 122131.
[43] L. Guo, D. Zhao, J. Xu, M.O. Tokhi, H.R. Karimi, Predicting unsteady heat-fluid interaction features and nonlinear acoustic behaviors in standing-wave thermoacoustic engines using unsteady RANS, LES and hybrid URANS/LES methods, Int. Commun. Heat Mass Transfer 142 (2023) 106617.
[44] Z. Tian, W. Zheng, X. Li, L. Zheng, Y. Jiang, Numerical investigation on condensation heat transfer performance of mixed hydrocarbon refrigerant in spirally tubes, Int. J. Refrig. 139 (2022) 13–24.
[45] Z. Yu, Q. Li, X. Chen, F. Guo, X. Xie, J. Wu, Investigation on the oscillation modes in a thermoacoustic Stirling prime mover: mode stability and mode transition, Cryogenics 43 (12) (2003) 687–691.
[46] G. Chen, L. Tang, B. Mace, Z. Yu, Multi-physics coupling in thermoacoustic devices: A review, Renewable Sustainable Energy Rev. 146 (2021) 111170.
[47] Z. Tian, W. Zheng, J. Guo, Y. Jiang, Z. Liang, X. Mi, Fundamental research on the condensation heat transfer of the hydrocarbon-mixture energy in a spiral tube described by a universal model using flow pattern based and general modes, Energy 296 (2024) 131019.
[48] Z. Tian, W. Zheng, J. Guo, Y. Wang, L. Wang, J. Chen, Y. Jiang, Experimental analysis on the flow patterns and conversion mechanisms of condensing flow with non-azeotropic mixtures in spiral tube, Exp. Therm Fluid Sci. 111245 (2024).
[49] G. Penelet, V. Gusev, P. Lotton, M. Bruneau, Experimental and theoretical study of processes leading to steady-state sound in annular thermoacoustic engines, Phys. Rev. E 72 (1) (2005) 016625.
[50] G. Chen, L. Tang, Z. Yu, B. Mace, Mode transition in a standing-wave thermoacoustic engine: A numerical study, J. Sound Vib. 504 (2021) 116119.
[51] J. Fu, J. Shu, F. Zhou, L. Zhong, J. Liu, B. Deng, Quantitative analysis on the effects of compression ratio and operating parameters on the thermodynamic performance of spark ignition liquefied methane gas engine at lean burn mode, Fuel 263 (2020) 116692.

[52] S. Zare, A. Tavakolpour-Saleh, Predicting onset conditions of a free piston Stirling engine, Appl. Energy 262 (2020) 114488.
[53] A. De Waele, Basic treatment of onset conditions and transient effects in thermoacoustic Stirling engines, J. Sound Vib. 325 (4–5) (2009) 974–988.
[54] L. Guo, D. Zhao, L. Cheng, X. Dong, J. Xu, Enhancing energy conversion performances in standing-wave thermoacoustic engine with externally forcing periodic oscillations, Energy 130634 (2024).
[55] G. Chen, L. Tang, B.R. Mace, Bistability and triggering in a thermoacoustic engine: A numerical study, Int. J. Heat Mass Transfer 157 (2020) 119951.
[56] H. Sayama, Introduction to the modeling and analysis of complex systems, Open SUNY Textbooks (2015).
[57] J. Tan, J. Wei, T. Jin, Onset and damping characteristics of a closed two-phase thermoacoustic engine, Appl. Therm. Eng. 160 (2019) 114086.
[58] K. Kashinath, I.C. Waugh, M.P. Juniper, Nonlinear self-excited thermoacoustic oscillations of a ducted premixed flame: bifurcations and routes to chaos, J. Fluid Mech. 761 (2014) 399–430.
[59] H. Chaté, G. Grinstein, L.-H. Tang, Long-range correlations in systems with coherent (quasi) periodic oscillations, Phys. Rev. Lett. 74 (6) (1995) 912.
[60] S. Tao, Z. Li, X. Li, J. Xu, E. Luo, G. Chen, On the nonlinear dynamic characteristics of forced acoustic oscillations in a heat-driven thermoacoustic engine, Nonlinear Dyn. 1–16 (2024).
[61] S. Backhaus, G.W. Swift, A thermoacoustic-Stirling heat engine: Detailed study, J. Acoust. Soc. Am. 107 (6) (2000) 3148–3166.
[62] D. Gedeon, DC gas flows in Stirling and pulse tube cryocoolers, in, Cryocoolers 9, Springer (1997) 385–392.
[63] J. Xu, J. Hu, Y. Sun, H. Wang, Z. Wu, J. Hu, S. Hochgreb, E. Luo, A cascade-looped thermoacoustic driven cryocooler with different-diameter resonance tubes, Part II: Experimental Study and Comparison, Energy 207 (2020) 118232.
[64] C. Yan, Y. Zhang, J. Qiu, Y. Chen, X. Wang, W. Dai, M. Ma, H. Li, E. Luo, Numerical and experimental study of partly tapered pulse tube in a pulse tube cryocooler, Int. J. Refrig. 120 (2020) 474–480.
[65] R. Yang, J. Wang, E. Luo, Revisiting the evaporative Stirling engine: The mechanism and a case study via thermoacoustic theory, Energy 273 (2023) 127282.
[66] L. Xiao, K. Luo, E. Luo, J. Xu, A. Summary, Dynamic and thermodynamic analysis of thermoacoustic and Stirling systems based on time-domain acoustic-electrical analogy, Appl. Energy 347 (2023) 121377.